



Full Text View

[Volume 31, Issue 12 \(December 2001\)](#)

Journal of Physical Oceanography

Article: pp. 3476–3495 | [Abstract](#) | [PDF \(2.46M\)](#)

Buoyancy Forcing by Turbulence above Rough Topography in the Abyssal Brazil Basin*

Louis C. St. Laurent, John M. Toole, and Raymond W. Schmitt

Woods Hole Oceanographic Institution, Woods Hole, Massachusetts

(Manuscript received August 17, 2000, in final form May 7, 2001)

DOI: 10.1175/1520-0485(2001)031<3476:BFBTAR>2.0.CO;2

ABSTRACT

Observations of turbulent dissipation above rough bathymetry in the abyssal Brazil Basin are presented. Relative to regions with smooth bathymetry, dissipation is markedly enhanced above rough topography of the Mid-Atlantic Ridge with levels above bathymetric slopes exceeding levels observed over crests and canyon floors. Furthermore, mixing levels in rough areas are modulated by the spring–neap tidal cycle. Internal waves generated by barotropic tidal flow over topography are the likely mechanism for supplying the energy needed to support the observed turbulent dissipation.

A model of the spatial and temporal patterns in the turbulent dissipation rate is used to constrain the diapycnal advection in an inverse calculation for the circulation in an area of rough bathymetry. This inverse model uses both beta-spiral and integrated forms of the advective budgets for heat, mass, and vorticity, and contains sufficient information to resolve the full three-dimensional flow. The inverse model solution reveals the presence of a buoyancy forced circulation driven by mixing in abyssal canyons. On isopycnals above the level of fracture-zone crests near the Mid-Atlantic Ridge, the flow is westward and fluid is downwelled toward greater density. Along deeper isopycnals, fluid is carried eastward and upwelled in canyons. The divergence of diapycnal mass flux is a significant forcing mechanism for this circulation. These results suggest that mixing in abyssal canyons plays an important role in the circulation of abyssal waters.

Table of Contents:

- [Introduction](#)
- [Observations](#)
- [Inverse model](#)
- [Results](#)
- [Discussion](#)
- [REFERENCES](#)
- [FIGURES](#)

Options:

- [Create Reference](#)
- [Email this Article](#)
- [Add to MyArchive](#)
- [Search AMS Glossary](#)

Search CrossRef for:

- [Articles Citing This Article](#)

Search Google Scholar for:

- [Louis C. St. Laurent](#)
- [John M. Toole](#)
- [Raymond W. Schmitt](#)

1. Introduction

The densest waters found in the ocean interior are formed at several high-latitude sites where atmospheric forcing causes surface water temperature and salinity conditions to match those of the deepest waters. These waters spill into the abyss and

are carried equatorward by a system of deep boundary currents (DBC). This view was outlined by [Stommel \(1957\)](#), and a model proposed by [Stommel and Arons \(1960\)](#) described a simple set of dynamics that link the DBCs to a weak interior circulation. Being far removed from the wind-driven Ekman layer, flow in the abyss is driven by buoyancy forcing. Lacking any information on the buoyancy forcing, Stommel and Arons calculated the circulation resulting from uniform upwelling. Under this scenario, poleward flow dominates the interior. However, early experiments by [Stommel et al. \(1958\)](#) demonstrated the tendency for zonal flow when the deep interior is characterized by a strong zonal gradient in the magnitude of buoyancy forcing. Specifically, the Stommel et al. experiments showed that zonal currents would transport mass between the deep western boundary current and isolated sources of upwelling to the east, with meridional motions in the interior inhibited by the absence of buoyancy forces.

The Stommel–Arons model is still central to our view of the abyssal circulation problem, and the important role of buoyancy forcing in the abyss is not questioned. Several studies have attempted to estimate the mixing rates responsible for abyssal buoyancy forcing. In particular, measurements of flow through deep passages have been used to formulate closed heat and mass budgets for semienclosed basins. Such heat–mass budgets have been the primary means of assessing abyssal mixing rates, and vertical diffusivities of $k_\rho \approx (1-10) \times 10^{-4} \text{ m}^2 \text{ s}^{-1}$ have been reported in the North and South Atlantic ([Saunders 1987](#); [Whitehead and Worthington 1982](#)), the South Pacific ([Roemmich et al. 1996](#)), and the Indian Ocean ([Barton and Hill 1989](#)). These mixing rates are up to several orders of magnitude larger than typical thermocline values. In contrast to the mixing rates implied by abyssal budgets, direct observations of dissipation over abyssal plains suggest that diffusivities there are comparable to thermocline diffusivity levels of $k_\rho \approx 1 \times 10^{-5} \text{ m}^2 \text{ s}^{-1}$ ([Toole et al. 1994](#); [Kunze and Sanford 1996](#)). Instead, the larger mixing rates needed to reconcile the budget estimates seem to occur near rough bathymetry, as suggested by several studies ([Toole et al. 1994, 1997a](#); [Polzin et al. 1997](#)).

The focus of the present work is the South Atlantic, where the densest waters of the global ocean are formed in the Weddell Sea off Antarctica. These waters, so-called Antarctic Bottom Water (AABW), flow northward along the western side of the Argentine Basin, reaching the Brazil Basin via the deep passages of the Vema and Hunter Channels. The isotherm bounding the water colder than about 1°C potential temperature intersects the seafloor within the basin, such that the coldest class of AABW does not exit the Brazil Basin adiabatically. The diffusion of heat driven by turbulent mixing provides the buoyancy needed to upwell this water. The Brazil Basin budget of AABW was considered by [Hogg et al. \(1982\)](#) and revisited by [Morris et al. \(2001\)](#). These investigations indicated that a basin-average vertical diffusivity of $(2-4) \times 10^{-4} \text{ m}^2 \text{ s}^{-1}$ was necessary to close the basin's heat and mass budgets.

However, as demonstrated by the experiments of [Stommel et al. \(1958\)](#), the structure of the interior flow is dependent on the specific distribution of deep sources and sinks of buoyancy, and budget studies give only spatially integrated estimates of buoyancy forcing. To investigate how spatial patterns of mixing influence flow in the abyss, a combined microstructure observation program and tracer dispersion experiment was started during 1996: the Brazil Basin Tracer Release Experiment (BBTRE).

Full depth microstructure data from the Brazil Basin were collected during January 1996 and April 1997. A free-falling, autonomous instrument platform called the high resolution profiler was used (HRP: [Schmitt et al. 1988](#)). The collective microstructure observations spanned nearly 30° longitude, covering the western basin and extending to the fracture zones (FZs) of the Mid-Atlantic Ridge (MAR). A preliminary presentation of microstructure-derived dissipation rates from the 1996 survey was given by [Polzin et al. \(1997\)](#), and data from the 1997 survey were discussed by [Toole et al. \(1997b\)](#). While these previous reports have focused on the estimation of turbulent diffusivities for the deep water of the Brazil Basin, the focus here will be to assimilate the dissipation data into an inverse model for the steady-state circulation.

The tracer dispersion experiment also began during January 1996 with an injection of 110 kg of sulfur hexafluoride at 4000-m depth, near 21.5°S , 18.5°W . The initial tracer plume was neutrally buoyant along the $\sigma_4 = 45.94 \text{ kg m}^{-3}$ isopycnal. This density surface is 500 to 1000 m above the FZ bathymetry at the longitude of the injection but deepens and intersects the seafloor about 400 km to the east. Tracer inventories were conducted during April 1997 (14 months postinjection) and March 1998 (26 months postinjection). Details of the tracer's dispersion are given by [Ledwell et al. \(2000\)](#) and will generally not be further described here. However, the tracer results compliment the microstructure-derived estimates, and relevant comparisons will be cited throughout this report.

The circulation problem will be posed in terms of flow in layers bounded by isopycnal surfaces along which potential density σ is constant. We will use a form of the scalar conservation equations described by [McDougall \(1987, 1995\)](#), where the lateral gradients are evaluated along isopycnal surfaces. This density coordinate system simplifies the analysis of mixing mechanisms, while still retaining the conventional vertical direction $\hat{\mathbf{z}} = \mathbf{g}/|\mathbf{g}|$. In this coordinate system, each isopycnal of the steady-state density field is specified as a two-dimensional function for the layer interface $z_i(\mathbf{x})$, and flow will be described by the conventional lateral components $\mathbf{u} = (u, \mathbf{v})$. However, the vertical component of flow is described by a new variable called the diapycnal advection, $w_* = (w - \mathbf{u} \cdot \nabla z_i)$. The diapycnal advection is the vertical component of flow

through (not normal to) isopycnals and the vertical motion that is caused by a divergent buoyancy flux. An expression for diapycnal advection can be derived from the equation for buoyancy along an isopycnal (Pedlosky 1996). An approximate expression for diapycnal advection in the ocean interior (away from surface buoyancy forcing) is

$$w_* N^2 \cong -\frac{\partial J_b}{\partial z}, \quad (1)$$

where N^2 is the buoyancy gradient and J_b is the buoyancy flux due to turbulence. In this expression, terms representing lateral fluxes of buoyancy have been neglected. The neglected terms include the cabbeling and thermobaric effects described by McDougall (1987), which are assumed to be small where fronts and intrusions are absent. Additionally, Garrett (2001) shows that terms related to isopycnal slope and curvature also arise in the full equation for w_* , which we expect to be negligible outside of a thin bottom boundary layer.

In much of the flow domain, geostrophic dynamics will be assumed and the circulation problem will be constrained through the use of the inviscid potential-vorticity equation

$$\beta v = \frac{f}{h} \mathbf{u} \cdot \nabla h + \frac{f}{h} (w_*(z_u) - w_*(z_l)), \quad (2)$$

where h is the thickness of the density layer, and (z_u, z_l) denote the upper and lower bounding isopycnal surfaces. The above expression is the density-layered version of the Stommel and Schott (1977) beta-spiral equation and is discussed by McDougall (1988) and Hautala and Riser (1993). It permits solution of the reference-level velocity problem by linear inversion when the geopotential-anomaly field has been measured. The diapycnal-advection term can modify the potential vorticity budget by vortex stretching of fluid columns, and this diabatic term is related to the divergence of buoyancy flux through (1). During mixing events, vertical exchanges of buoyancy are accompanied by dissipation of turbulent kinetic energy (TKE), and the energy budget for an ensemble of turbulent events is

$$(1 - R_f)J_b + R_f \epsilon = 0, \quad (3)$$

where ϵ is the dissipation rate, and R_f is the efficiency of the mixing. The TKE budget expressed in (3) assumes steady-state and homogeneous statistics of the Reynolds stress tensor. This equation is discussed by Osborn (1980), and an expression for the eddy diffusivity is readily derived by substituting $J_b = -k_\rho N^2$ into (3):

$$k_\rho = \left(\frac{R_f}{1 - R_f} \right) \left(\frac{\bar{\epsilon}}{N^2} \right). \quad (4)$$

The fraction $\Gamma = R_f(1 - R_f)^{-1}$ (equivalently $\Gamma = -J_b/\epsilon$), the ratio of buoyancy flux to energy dissipated, is typically taken to be $\leq 20\%$ for stratified turbulence. With use of (1) and (3), the diapycnal advection can be expressed as

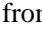
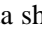
$$w_* \cong N^{-2} \frac{\partial(\Gamma \bar{\epsilon})}{\partial z}. \quad (5)$$

Previous attempts to examine mixing rates and diapycnal velocities in inverse models have been done for both box models of the advective budgets (e.g., Zhang and Hogg 1992) and beta-spiral inversions (e.g., Hautala and Riser 1993). These inversions all rely on either integrated property budgets (box inversions) or differential property budgets (beta-spiral inversions), and the mixing rates and diapycnal velocity estimates are determined through the divergences of lateral fluxes. This form of mixing-rate estimation is highly sensitive to small uncertainties in the advective terms, as discussed by Wunsch (1996). The inverse model used in this study resembles the model of Fukumori (1991) in that both integrated and differential budgets are used. In this manner, mass conservation and the thermal advection are closed in volume-integrated cells, while the advection of potential vorticity is examined in the differential form of the beta-spiral equation.

The description of the turbulent dissipation observed during BBTRE will begin in section 2. There, we will discuss spatial and temporal features of mixing. In section 3, an inverse model for estimating the circulation will be formulated. There we will describe the governing equations for the model (section 3a), the model for the time-mean dissipation (section 3b), the treatment of data (section 3c), and the details of the linear inverse (section 3d). The results of the inverse calculation are presented in section 4. There we present estimates of both shallow (section 4a) and deep (section 4b) flow, canyon flow (section 4c), and deep upwelling and mixing efficiency (section 4d). A discussion of the estimated circulation will be given

2. Observations


In the period between January 1996 and April 1997, two microstructure surveys were made in the Brazil Basin. During the first cruise, January through February 1996, a 75 station HRP survey consisting of two section legs covered a region extending from the continental slope regions off Rio de Janeiro (24°S) and Recife (11°S) to the western edge of the MAR (16°W at 21°S) where the tracer was injected. A second survey was carried out in March and April of 1997. An irregular grid of HRP stations was occupied over the region (19°–25°S, 12°–23°W). The primary focus of the 1996 survey was the spatial variability of mixing levels, and a report on the observed variability is given by [Polzin et al. \(1997\)](#).

The present work will focus on dissipation data collected over the fracture zones east of 25°W. This dataset consists of 87 stations from the 1997 survey and an additional 42 stations from the 1996 survey ([Fig. 1](#) ). All profiles consist of conventional hydrographic variables (e.g., Θ , S , U , V) in addition to microstructure, and generally extend from the surface mixed layer to within 20 m of the bottom. The bathymetric data shown in [Fig. 1](#)  were derived from satellite measurements of the marine gravity field ([Smith and Sandwell 1997](#)). The map clearly shows the network of FZs leading east to the MAR. This system of FZs is characterized by a series of canyons bounded latitudinally by crests that rise up to 1 km above the canyon floors. The canyon of an unnamed FZ between 21° and 22°S was heavily sampled during the 1997 survey. Observations from this canyon will receive careful attention in [section 4c](#).

The dissipation estimates were derived from observations of velocity microstructure. Only two components of the strain tensor are measured and isotropy is assumed to express the dissipation rate as


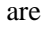
$$\epsilon = (15/4)(\langle u_z^2 \rangle + \langle v_z^2 \rangle).$$

The use of the isotropy assumption cannot be justified through inspection of the available field data, but studies have shown that the isotropic relation provides a good estimate of dissipation ([Yamazaki and Osborn 1990](#)). The precise details of the dissipation calculation are discussed by [Polzin and Montgomery \(1996\)](#).

A summary of the observed deep-dissipation data was made by collapsing the latitudinal spread of the stations ([Fig. 2](#) ). To simplify the presentation, only the depth range deeper than 2000 m is shown. The dissipation data were depth averaged into 100-m intervals, and individual profiles are shown as columns of binned dissipation. Since the latitudinal extent of the survey has been collapsed, no particular section of bathymetry is entirely appropriate. Instead, two classes of representative bathymetry are shown: the bathymetry of FZ crests and the bathymetry of canyon floors, as sampled from the latitude range 21°–23°S.

Within about 500 m of the bottom, there is an enhancement of dissipation by up to two orders of magnitude over values observed at middepth. Enhanced dissipation generally occurs between the level of FZ crests and canyon floors. Thus, the largest mixing rates are observed in canyons.

a. Spatial variability

The spatial patterns of enhanced dissipation apparent in [Fig. 2](#)  suggest that variability of dissipation is associated with the different sloping regions that characterize the crest–canyon system of the FZs. This also suggests that height above bottom (h_{ab}) may serve as a better coordinate than depth for examining the spatial distribution of ϵ . This approach was adopted, and the available profiles of ϵ were classified according to the meridional slope of the local bathymetry $Z_b(x, y)$. HRP stations were categorized as being FZ crests ($\partial_y Z_b \cong 0$, $\partial_{yy} Z_b < 0$), canyon floors ($\partial_y Z_b \cong 0$, $\partial_{yy} Z_b > 0$), or sloping regions ($\partial_y Z_b \neq 0$). The profile data, classified in this manner, are shown as functions of h_{ab} in [Fig. 3](#) . Each ensemble profile results from data that has been vertically averaged into 100-m bins. Auto-lag-correlation analysis of ϵ profiles shows zero crossings at 20-m vertical separations, so each 100-m bin contains five degrees of freedom. The 95% confidence interval of each bin was calculated using the “boot strap” Monte Carlo method ([Efron and Gong 1983](#)). Dissipation decreases with height in each of the three classes, and all profiles reach background levels of dissipation, $\epsilon \cong 3 \times 10^{-10}$ W kg⁻¹, at heights above bottom greater than 1000 m. The slope profile is notably different from the other two, in both the magnitude of the maximum dissipation and the scale of decay. The slope profile has a bottom value of $\epsilon \cong (3-9) \times 10^{-9}$ W kg⁻¹ and decays with an e -fold scale of (150 ± 50) m. The crest and canyon profiles peak at $\epsilon \cong (2-5) \times 10^{-9}$ W kg⁻¹ and decay over a larger scale, (500 ± 100) m.

b. Temporal variability

In addition to this spatial structure, temporal variability also exists in the dissipation data. Daily averages of dissipation data roughly modulate with the spring–neap cycle of tidal currents. This correlation is most evident when the dissipation profiles are vertically integrated, and a comparison between integrated ϵ and tidal current speed is made using estimates of barotropic tidal velocity produced by the TPXO model of [Egbert et al. \(1994\)](#) (Fig. 4 \bullet –). For the time intervals where dissipation data were available, the TPXO model was used to produce velocity estimates at the latitude and longitude appropriate for each HRP station.

In both 1996 and 1997 comparisons, profiles of $\rho\epsilon$ were integrated up from the local bottom to $h_{\text{ab}} = 2000$ m, and all profiles were time binned in 24-h intervals and averaged. The modulation of integrated dissipation follows the phase of the spring–neap tidal cycle closely, and a one day lead of the tidal signal is consistent within the statistical spread of the data. While the correlation between the two records is quite low for the 1996 data, near 0.3, the correlation coefficient for the 1997 data is 0.7. Furthermore, this comparison uses only the tidal record reconstructed along the survey track, though the dissipation is possibly influenced by tidal beams that have radiated from other sites. We regard the temporal fluctuations in the dissipation record as suggestive of tidal forcing, and explore this possibility further in [section 3b](#).

3. Inverse model

a. Model equations

We focus here on the ocean abyss and make the a priori assumption that the diabatic terms in the governing equations are significant. All dynamical equations will be cast in terms of flow along and across isopycnals. The dynamically relevant density variable for this analysis is neutral density (γ_n ; [Jackett and McDougall 1997](#)): the neutral density coordinates are everywhere parallel to the locally defined potential density. Preliminary examination of multiple-year hydrographic data revealed that the temporal variation of the isopycnal-height field was negligible ([Ledwell et al. 2000](#)). Therefore, we will assume that the density field can be regarded as steady over the 14-month period spanned by the observations.

The flow regime is divided into a series of density layers, each characterized by a layer thickness $h(x, y)$. In these layers, geostrophic advection is related to isobaric gradients of geopotential anomaly (Ψ) by

$$\mathbf{u} = \hat{\mathbf{z}} \times \frac{\nabla\varphi}{f} + \mathbf{u}_0, \quad (6)$$

where \mathbf{u}_0 is a reference level velocity. Thus, the advection of potential vorticity through a density layer, as previously stated in (2), may be expressed in the form

$$\begin{aligned} \frac{h_x}{h}u_0 + \left(\frac{h_y}{h} - \frac{\beta}{f}\right)v_0 + \frac{1}{h}(w_*(z_u) - w_*(z_l)) \\ = -u_r \frac{h_x}{h} - v_r \left(\frac{h_y}{h} - \frac{\beta}{f}\right), \end{aligned} \quad (7)$$

where (u_r, v_r) are the components of relative geostrophic velocity given by $(u - u_0, v - v_0)$ in (6). Thus, the problem of determining the lateral flow \mathbf{u} is reduced to determining the reference level velocity, that is, the vertical integration constants (u_0, v_0) of a thermal-wind balance.

In layers where flow encounters topography, the use of geostrophic balance is questionable. A modified momentum balance, such as that of the bottom Ekman layer, may be called for in regions where a density layer comes within $h_{\text{ab}} \cong 100$ m of the bottom. Additionally, the difficulty of defining the geopotential anomaly along pressure surfaces interrupted by bathymetry severely limits the practical use of (6) and (7) in deep layers. For these reasons, it is necessary to employ additional dynamical constraints on the flow. This is achieved through the use of integrated advective budgets for mass,

$$\begin{aligned} & \iint dy dz (u|_x^{x+\gamma}) + \iint dx dy (v|_y^{y+\Delta}) \\ & + \iint dx dy (w_*|_{z_l}^{z_u}) = 0, \end{aligned} \quad (8)$$

and for potential temperature

$$\begin{aligned} & \iint dy dz (u\Theta'|_x^{x+\gamma}) + \iint dx dy (v\Theta'|_y^{y+\Delta}) \\ & + \iint dx dy (w_*\Theta'|_{z_l}^{z_u}) \\ & = \iint dy dz (\kappa\Theta_x|_x^{x+\gamma}) + \iint dx dz (\kappa\Theta_y|_y^{y+\Delta}) \\ & + \iint dx dy (k_\rho\Theta_z|_{z_l}^{z_u}). \end{aligned} \quad (9)$$

The integrated expressions (8) and (9) are bounded in a control volume of zonal and meridional extent (γ , Δ), and vertically bounded in a density layer by the surfaces $z_u(x, y)$ and $z_l(x, y)$. In the temperature advection equation, Θ' is the temperature anomaly relative to the mean temperature in each cell, and κ and k_ρ are the respective isopycnal and diapycnal diffusivities. Since (8) and (9) assume nothing about the nature of the momentum balance, their applicability is not limited to conditions of geostrophic balance. However, without any model for the momentum balance, the components of the lateral flow in (8) and (9) must be treated as unknowns at all depths, in contrast to (7), which relates the velocity at all depths to the single component pair (u_0, \mathbf{u}_0).

The diffusivity for isopycnal mixing, κ , is treated as an unknown parameter in the inverse model. Relations for the diapycnal diabatic terms are expressed using the dissipation rate with the use of (4) and (5). For use in the inverse model, the mixing efficiency parameter Γ is treated as constant, $\Gamma_0 = 0.20 \pm 0.04$. This allows us to specify the diapycnal diffusivity for turbulence as

$$k_\rho \cong \frac{\Gamma_0}{N^2} \bar{\epsilon}, \quad (10)$$

and the diapycnal advection as

$$w_* \cong \frac{\Gamma_0}{N^2} \frac{\partial \bar{\epsilon}}{\partial z}. \quad (11)$$

We emphasize that (10) and (11) are approximations, where a constant mixing efficiency has been assumed. While oceanic observations of turbulence from well-stratified regions suggest $\Gamma_0 \cong 0.2$ ([Moum 1996](#); [St. Laurent and Schmitt 1999](#)), observations from fjords suggest $\Gamma \cong 0.05$ ([Stigebrandt and Aure 1989](#)). Additionally, laboratory measurements of turbulence suggest $0.05 < \Gamma < 0.25$ characterizes the variation of mixing efficiency over a wide range of Reynolds, Richardson, and Froude numbers ([Ivey and Imberger 1991](#); [Huq and Britter 1995](#)). In our inverse model estimates, we accept that using $\Gamma_0 = 0.20 \pm 0.04$ may lead to a specification of k_ρ that is biased high. The use of a constant mixing efficiency in (11) is more problematic, as variations in Γ with depth will not only influence the magnitude of the w_* estimate, but also the sign ($w_* > 0$ for upwelling, $w_* < 0$ for downwelling). For this reason, w_* is regarded as an unknown in the inverse model, and (11) serves as a ‘‘constraint’’ in the inversion. In this manner, (11) provides an a priori estimate, while full inversion of (7), (8), and (9) determines the best estimate of w_* . The use of constraints in inverse models is discussed by [Menke \(1989\)](#) and [Wunsch \(1996\)](#).

In expressions (10) and (11), $\bar{\epsilon}$ is meant to denote some suitably averaged function of the dissipation data. Averaging over

multiple profiles is necessary to achieve statistical stability in the mean dissipation estimates. Since our inverse model utilizes the steady-state forms of the advective budgets, we seek an averaging procedure that yields an estimate of the time-mean dissipation rate. Additionally, the averaging procedure should preserve the dependence of ϵ on bathymetric class, as previously described in [section 2](#). We now discuss such a model for the time-mean dissipation.

b. Model for the turbulent dissipation

Spatial and temporal variations in the observed dissipation data were described in [sections 2a and 2b](#). These variations are not random, and simple arithmetic averaging may alias modes of variability in a manner that will produce biased estimates of mean dissipation. Estimates of spatially averaged dissipation are sensitive to the layout of bathymetric crests, slopes, and canyons in that ϵ levels above slopes can exceed levels above crests and canyon floors. Similarly, estimates of time-averaged dissipation are sensitive to the phase of the spring–neap tidal cycle, as ϵ levels are maximum near spring tide and minimal near neap tide. Due to the logistics of the tracer component of the experiment, canyon sites were favored during data collection, and three of five weeks of sampling occurred during neap tides. Thus, simple averages of the observed dissipation data are biased low relative to the true temporal and spatial mean. We therefore rely on simple modeling to recover an unbiased estimate of mean dissipation.

First, we consider the fortnightly modulation of the dissipation with the barotropic tidal current. Traditionally, frictional boundary-layer dynamics are assumed as the mechanism for tidally driven dissipation. The energy dissipated in the frictional boundary layer is estimated as $\epsilon = \rho_0 c_d |u|u^2$, where $c_d \simeq 0.0025$ is the drag coefficient and u is the barotropic velocity of flow. Taking $u = 0.02 \text{ m s}^{-1}$, the tidal dissipation in the frictional boundary layer is $W_f \simeq 0.02 \text{ mW m}^{-2}$. This is two orders of magnitude smaller than the integrated dissipation occurring between the bottom and a height of 2000 m. It is further noted that HRP profiles seldom extend close enough to the bottom to sample the frictional boundary layer, which is typically 1 to 10 m thick.

In contrast to bottom friction, the internal waves generated by tidal flow over rough bathymetry radiate energy upward, away from the bottom. Instabilities in the internal wave field act to transfer some of this energy to the small scales where it is dissipated by viscosity. Thus, internal waves provide an additional, though indirect, mechanism by which tidal energy is dissipated. The internal wave generation problem of flow over bottom bathymetry is well known, and a general discussion of steady flow “lee wave” generation is given by [Gill \(1982\)](#). Internal waves produced by tidal flow are termed “internal tides,” and unlike lee waves, internal tides have intrinsic frequencies equal to those of the barotropic tides. Internal tide generation models are discussed by [Baines \(1982\)](#), who shows that the energy flux associated with the internal tide radiated from linear slope topography scales as $E_f \simeq K\rho_0 Nu^2 h^2$, where N is the buoyancy frequency, u is the barotropic tidal velocity, h is the depth, and K is a parameter that depends on the height of the topography relative to the water depth and the geometry of the slope. This scaling is valid for linear slopes of arbitrary steepness, though the particular value of K depends on whether the slope is supercritical (slope steeper than the beam of radiated waves) or subcritical (slope less steep than waves). For the case of subcritical topography, [Bell \(1975\)](#) shows that the energy flux for topography of arbitrary shape scales as $E_f \simeq k\rho Nu^2 d^2$, where (k, d) are the wavenumber and height of a topographic obstacle. Using this scaling as a lower bound, an energy flux of $E_f \simeq 1\text{--}10 \text{ mW m}^{-2}$ is likely to characterize the internal tide generated across the FZs. This value for energy flux is the same scale as the observed integrated dissipation values to a height of 2000 m above the topography.

Assuming that the energy available for dissipation scales as the energy flux of the internal tide, a model for the dissipation was developed in several steps. First, the data were temporally dealiased assuming that $\epsilon \simeq au(t)^2$, where $u(t)^2$ is the squared barotropic tidal speed that has been smoothed with a one day running average. The long-term average for $\overline{u^2}$ was computed over the 14-month period between the 1996 and 1997 surveys using tidal velocity estimates at the central site (21° S , 18.5° W). The resulting temporally dealiased dissipation data are a function of spatial variables only. The second procedure in the modeling was to simplify the spatial dependence. This was done by grouping the data into the three bathymetric classes: FZ crests, canyons, and the slopes between them. The resulting model for dissipation is dependent only on $h_{\text{ab}}(\mathbf{x})$,

$$\overline{\epsilon}(h_{\text{ab}}(\mathbf{x})) = (\overline{u^2}/u(t)^2) \langle \epsilon(\mathbf{x}, h_{\text{ab}}(\mathbf{x}), t) \rangle, \quad (12)$$

where angle brackets represent the average over an ensemble of profiles associated with a bathymetric class.


c. Treatment of data

The dynamics described in [section 3a](#) can be employed in an inverse model where the observed density field $(h(x, y), N^2)$, geopotential-anomaly field $\Phi(x, y, p)$, temperature field $\Theta(x, y, z)$, and modeled dissipation $\epsilon(h_{\text{ab}}(\mathbf{x}))$ are used to solve for the

unknowns (\mathbf{u} , w_* , κ). The geometry of the inversion grid needs to accommodate both the finite element nature of the beta-spiral vorticity balance (7) and control-volume cells for (8) and (9). This is done using a staggered grid of nested control-volume cells. For each density layer, cells are assigned to serve as control volumes with the integrated components of lateral velocity constrained on each of the lateral walls and diapycnal velocities constrained on the upper and lower bounding density interfaces.

The 1997 HRP survey data provided the hydrographic fields. The temperature and salinity data were first used to calculate isobaric maps of geopotential anomaly relative to 2000 dbar. These fields were modeled using a polynomial fit over the survey domain with the form $\Phi(X, Y) = \Phi_0 + \Phi_x X + \Phi_y Y + \Phi_{xx} X^2 + \Phi_{xy} XY + \Phi_{yy} Y^2$, where (X, Y) are Cartesian coordinates and $\Phi_{(\cdot)}$ are the coefficients of the fit. The second-order polynomial fit was found to filter tidal displacements in the density field (St. Laurent 1999). The gradient of the fit is used with (6) to give estimates of the geostrophic flow relative to 2000 m. This reference level was chosen based on ideas about basin-scale water masses, with 2000 m being roughly between northward flowing intermediate water and southward flowing North Atlantic Deep Water (NADW). The hydrographic data were sorted into layers of neutral density, and polynomial fits were used to give quasi-analytic expressions for $\Theta(x, y)$, $\Theta_z(x, y)$, $h(x, y)$, and $N^2(x, y)$ in each layer. This layered system comprises the static stratification field, which is used for the inversion. Vertical derivatives for N^2 and Θ_z and their associated uncertainty were calculated using the slopes from linear fits to the data. For each density layer, the linear fits were computed about the level of the bounding isopycnal over a depth interval comparable to the density layer thickness. Assignments of geostrophic shear for each layer were made through explicit reference to the isobaric surfaces used in the geopotential-anomaly calculation. Thus, the inverse domain is a layered system of hydrographic estimates on a staggered grid of nested cells. Various domain dimensions were explored, but the calculations discussed here cover 19° – 25° S, 14° – 22° W and six density layers, with $\gamma_n = 27.6 \text{ kg m}^{-3}$ (density units are suppressed hereafter) serving as the uppermost interface and the seafloor bathymetry serving as the lower boundary of the inverse domain. Each cell of the staggered grid has Mercator dimensions of $(0.5^\circ)^2$, and the altimetry-derived bathymetry data of Smith and Sandwell (1997) were subsampled onto this grid. The modeled dissipation data (12) were incorporated into the inverse domain by identifying each estimation point as a bathymetric crest, slope, or canyon. This was done through a classification scheme that utilizes both the first and second meridional derivatives of bathymetry, which were computed at two arc minute resolution.

Residuals between the fitted and observed density field are typically 20–50 m, assumed to be the result of tidal heaving, and an assessment of hydrographic noise was done using Monte Carlo methods. In particular, the influence of 50-m amplitude vertical displacements of the isopycnal-height field arising from tidal frequency motions was examined. To accomplish this, the observed isopycnal-height field was perturbed by a random field of Gaussian noise with 50-m standard deviation. The perturbed density field was then treated with the polynomial smoothing discussed above, and this smoothed but perturbed hydrography was used for the inversion. In this manner, 10 alternate realizations of the density field were produced, and an ensemble of inverse solutions was calculated.

Since the survey data were concentrated above several FZs along an irregular grid (Fig. 1 ) , some regions of the inverse domain correspond to regions that were sparsely sampled. There is no survey data in the northeast and southeast corners of the 19° – 25° S, 14° – 22° W inverse domain, so the mapped properties in these regions are poorly constrained. The inverse estimates in these sparsely sampled regions will receive minimal attention.

d. Linear algebraic equations

The fitted hydrographic fields and the dissipation data were used to assemble a linear system of coupled equations of the form $E_{ij}x_j + n_i = d_i$, where E_{ij} is the coefficient matrix of the terms in (7), (8), and (9) involving the unknowns $x_j = [u_0, \mathbf{u}_0, w_*, \kappa]^T$, plus the estimates $w_* \cong N^{-2} \Gamma_0 \partial \epsilon / \partial z$, which act as constraints. The vector d_i is the vector of observable terms, and n_i explicitly denotes the residuals of the inverse model fit. This linear system is solvable by least square methods that generally minimize the residuals of the model fit. A variety of inversion procedures are discussed by Wunsch (1996), and the Gauss–Markov estimator was chosen for the calculations needed here. This form of inversion produces an estimate of x_j that utilizes a priori knowledge of the statistics for x_j and n_i , which is done through a specification of covariance matrices. The covariance matrix of unknowns C_{jj} is taken to be the diagonal matrix composed of the variance quantities. A priori variance levels for the lateral flow and the lateral diffusivity were taken as $\langle (u - \bar{u})^2 \rangle \cong (0.01 \text{ m s}^{-1})^2$ and $\langle (\kappa - \bar{\kappa})^2 \rangle \cong (100 \text{ m}^2 \text{ s}^{-1})^2$. The assumed scale for the lateral flow is justified by float observations (Hogg and Owens 1999). The scale for the lateral diffusivity was derived from a mixing length estimate. Using an eddy kinetic energy of $1 \text{ cm}^2 \text{ s}^{-2}$ (Hogg and Owens 1999) and a deformation radius length scale of order 10 km suggests $u' / l' \cong 100 \text{ m}^2 \text{ s}^{-1}$. The variance levels for the diapycnal advection came directly from the statistics of the dissipation constraint (5). Along density surfaces well above

topography where mixing rates are weak, a typical variance level for diapycnal advection was $\langle (w_* - \bar{w}_*)^2 \rangle \simeq (1 \text{ m yr}^{-1})^2$. Along density surfaces closer to topography, variance levels were $\langle (w_* - \bar{w}_*)^2 \rangle \simeq (10\text{--}30 \text{ m yr}^{-1})^2$. A diagonal covariance matrix for the model residuals R_{ii} was constructed using an uncertainty analysis of the elements of d_i . For example, the scale for the residuals of the beta-spiral equations involves the error propagation of terms like $(\delta h)^2$, $(\delta h_x)^2$, and $(\delta h_y)^2$ in (7). The $\delta(\cdot)$ terms are calculated using the standard errors of the mapped hydrography, where the expressions for error propagation were derived using standard techniques (Bevington and Robinson 1992). Typical signal to noise ratios of the observed terms of the geostrophic model equations are $(|d_i|/\delta d_i) \simeq 1/5$ for the beta-spiral and heat equations and $(|d_i|/\delta d_i) \simeq 1$ for the mass and diapycnal advection constraints. The statistical uncertainties assigned to the ageostrophic advective budgets are $0.01 \times 10^6 \text{ m}^3 \text{ s}^{-1}$ and $1 \times 10^2 \text{ m}^3 \text{ }^\circ\text{C s}^{-1}$ for the mass and heat.

In addition to the statistical scalings provided by the two covariance matrices, several nonstatistical scalings are used to improve the rank of the inversion. The linear model is nondimensionalized by column scaling with a diagonal matrix of dimensional scales D_{jj} so that all elements of x_j are $O(1)$. Additionally, the rows of E_{ij} are scaled by the equation norms N_{ii} and the thermal advection equations are row scaled by the temperature contrasts T_{ii} of each control-volume cell. The later scaling accounts for the general decrease in temperature contrast as layers get deeper and is discussed by Zhang and Hogg (1992). Thus, the Gauss–Markov estimate for the nondimensional variables x'_j and the associated uncertainty $\delta x'_j$ are given by

$$\begin{aligned} x'_j &= \text{inv}(C'_{jj}{}^{-1} + E'_{ij}{}^T R'_{ii}{}^{-1} E'_{ij}) E'_{ij}{}^T R'_{ii}{}^{-1} d'_i, \\ \delta x'_j &= \text{inv}(C'_{jj}{}^{-1} + E'_{ij}{}^T R'_{ii}{}^{-1} E'_{ij})^{1/2}, \end{aligned} \quad (13)$$

where the scaled matrices are $E'_{ij} = N^{-1}_{ii} T^{-1}_{ii} E_{ij} D_{jj}$, $C'_{jj} = D^{-2}_{jj} C_{jj}$, $R'_{ii} = N^{-2}_{ii} T^{-2}_{ii} R_{ii}$, and $d'_i = N^{-1}_{ii} T^{-1}_{ii} d_i$.

4. Results

The matrix model for the six-layer system consisted of about 7000 equations for 3200 unknowns. In a series of initial calculations, lateral diffusivity κ was treated as constant along each density surface used in the inversion. Using this approach, the estimates of κ were inconsistent with the a priori estimates of $\kappa \simeq 100 \text{ m}^2 \text{ s}^{-1}$. Spatially variations of κ on isopycnals intersecting topography may account for this discrepancy. Additionally, diagnostic scaling with $\kappa \simeq 100 \text{ m}^2 \text{ s}^{-1}$ indicated that the primary thermal-advection balance in (9) occurs between the terms involving advection (both lateral and vertical) and the vertical diffusion term. For these reasons, terms involving the lateral diffusivity were dropped from the thermal-advection equations, leaving the three-dimensional flow field (\mathbf{u} , w_*) as the model unknowns. The singular value decomposition (SVD) of the scaled matrix E'_{ij} was calculated, and the parameter and data resolution matrices of the SVD are discussed by St. Laurent (1999).

a. Shallow flow

Diapycnal mixing in the layers shallower than 3000 m was weak and diffusivity estimates were $k_p = (\Gamma/N^2)\epsilon < 1 \times 10^{-4} \text{ m}^2 \text{ s}^{-1}$. Consequently, the diapycnal advection through these layers was also weak, with $|w_*| < 1 \text{ m yr}^{-1}$. Diabatic forcing of this magnitude plays a rather insignificant role in the determination of the lateral flow, as the diabatic term in (7) is typically less than 10% of the adiabatic stretching term represented by $\mathbf{u} \cdot (\nabla h/h)$. Therefore, the weak diabatic flow in these shallow layers is not discussed further.

Within the domain treated by the inversion, the bottom topography does not shoal less than 3000 m with the exception of a seamount in the southeast corner of the region. Thus, geostrophic dynamics were assumed valid everywhere in layers shallower than 3 km, and the combined use of the beta spiral with mass and temperature advection yielded an overdetermined system for the barotropic flow at each grid point. The estimated geostrophic flow fields for levels shallower than 3000 m, including the reference level, are shown in Fig. 5. The largest current speeds in these layers are 2 mm s^{-1} , and the mean speeds are around 0.5 mm s^{-1} . The flows in these layers are generally consistent with ideas about water mass circulation. Above and below a level of very weak flow ($\gamma_n = 27.83$, $z \simeq 2200 \text{ m}$), the intermediate water layer ($\gamma_n = 28.01$, $z \simeq 1400 \text{ m}$) flows in a northward direction, while the NADW layer ($\gamma_n = 28.06$, $z \simeq 2900 \text{ m}$) flows in a southward direction. The local nature of these flow domains makes detailed comparisons with previous results difficult, as most past

work has considered basin scales. [Durrieu De Madron and Weatherly \(1994\)](#) describe the Brazil Basin circulation of NADW and AABW water masses, but their observations do not cover the region considered in our study. [Reid \(1989\)](#) estimated net northward flow at $z = 2000$ m near 20°S , 20°W in his study of large-scale South Atlantic circulation. Also, [Speer et al. \(1995\)](#) describe a section at 22°S , 15°W with net eastward transport in the depth range between 1300 and 3200 m as part of the Namib Col Current, a feature not apparent in our data. However, the flows found here have qualitative similarity to flow estimates discussed by [Zhang and Hogg \(1992\)](#).

In [Fig. 5](#), an ensemble of 10 velocity estimates is plotted at each grid point. The spread of vectors at each point is the result of uncertainty in the determination of the reference-level flow due to ± 50 m noise in the isopycnal-height field. In many cases, the estimated variations are small and not apparent in the figures. The flow estimates are most sensitive in the northeast and southeast corners of the domain, where no stations were occupied. This sensitivity amounts to an uncertainty in flow direction not greater than $\pi/12$ radians. Statistical uncertainty in the magnitude of the flow field is typically $0.1\text{--}0.2$ mm s^{-1} , as assessed from standard error propagation techniques used with the polynomial fits to the geopotential-anomaly fields.

b. Deep flow

In the layers deeper than 3000 m, bottom bathymetry has a clear influence on the flow dynamics. In particular, proximity to the bottom is the controlling factor for the magnitude of the diabatic forcing. The vertical diffusivity characterizing these layers is $k_\rho \cong 1 \times 10^{-4} \text{ m}^2 \text{ s}^{-1}$ or greater, and this corresponds to an increased importance of the diabatic terms in the governing equations. The estimated lateral flow fields, with associated vertical diffusivities, are shown in [Figs. 6, 7, and 8](#). Flow in these layers is generally southward and westward, with average current magnitudes of $2\text{--}4 \text{ mm s}^{-1}$ and the faster currents occurring in the western portion of the region exceeding 5 mm s^{-1} . The influence of ± 50 m noise in the isopycnal-height field has also been evaluated, and the lateral flow is very stable to perturbations of this magnitude.

The neutral density range $28.12 < \gamma_n < 28.18$ ($45.88 < \sigma_4 < 45.96$) is of particular interest, because this density layer bounds the target isopycnal used for the tracer release, $\gamma_n = 28.16$ ($\sigma_4 = 45.94$). The tracer inventory made during the 1997 survey indicated that the tracer's center of mass was advected 130 km southwest over a period of 14 months, as reported by [Ledwell et al. \(2000\)](#). This is equivalent to a time average speed of 3.6 mm s^{-1} . The average velocity in the density layer $28.12 < \gamma_n < 28.18$, as estimated by the inversion for the region $22^\circ\text{--}25^\circ\text{S}$, $18.5^\circ\text{--}22^\circ\text{W}$, is $|\mathbf{u}| = (3 \pm 0.3) \text{ mm s}^{-1}$ in the direction $220^\circ\text{--}230^\circ$. Thus, the lateral flow estimate given by the inversion is consistent with the rate of lateral advection measured by the tracer. The calculated flow in these layers is also consistent with float observations made in this region during 1994–96, as reported by [Hogg and Owens \(1999\)](#). These estimates of flow are not consistent with the estimates of [Reid \(1989\)](#), who found northward flow near 20°S , 20°W at 4000 and 4500 m.

A detailed discussion of tracer- and microstructure-derived diffusivities for the target isopycnal is given by [Ledwell et al. \(2000\)](#). The tracer-derived result of $k_{\text{SF}_6} \cong 3 \times 10^{-4} \text{ m}^2 \text{ s}^{-1}$ compares well with the 95% confidence interval of the microstructure estimate, $k_\rho = (2.3 \pm 1) \times 10^{-4} \text{ m}^2 \text{ s}^{-1}$. The later estimate was made using the 14-month tracer concentration field as weighting in the spatial average, and is thus not representative of the larger diffusivities of $(5\text{--}10) \times 10^{-4} \text{ m}^2 \text{ s}^{-1}$ that occur east of the tracer patch. As is apparent in [Figs. 7 and 8](#), there is an order of magnitude increase in vertical diffusivity over the longitudinal extent of the inverse model region.

Diapycnal advection estimates were made on density surfaces, and these estimates are presented in [Figs. 9, 10, and 11](#). The $\gamma_n = 28.08$ ($\sigma_4 = 45.83$) surface is characterized by downward advection with mean $w_* = -3 \pm 1 \text{ m yr}^{-1}$; larger downward pumping occurs in the east. The deeper surfaces, $\gamma_n = 28.16$ ($\sigma_4 = 45.94$) and $\gamma_n = 28.20$ ($\sigma_4 = 45.98$) are characterized by larger values of advection, $|w_*| \cong 10 \text{ m yr}^{-1}$, with individual estimates having associated uncertainty of roughly 20%–40%. The $\gamma_n = 28.16$ surface was the target isopycnal for the tracer release experiment, and downward advection is estimated over the part of the domain occupied by the tracer patch. This is consistent with the 14-month tracer inventory, and a later 28-month inventory, both of which indicate that the tracer's center of mass sank relative to the target isopycnal ([Ledwell et al. 2000](#)).

Diapycnal advection through the eastern range of the tracer surface is upward, as it is for nearly all of the surfaces deeper than the $\gamma_n = 28.20$ surface. [Figures 10 and 11](#) show contoured fields of w_* that have been highly smoothed. Where ridge topography occupies each density layer there is no flow, and the contoured maps show estimates of w_* that have been averaged in $1^\circ \times 1^\circ$ cells, which often include regions blocked by topography. Estimates of upward advection in canyons exceed $w_* \cong 30 \text{ m yr}^{-1}$ and are as large as $w_* \cong 100 \text{ m yr}^{-1}$ in some local regions. In FZ canyons, eastward flow is

estimated with magnitude $0.4 \pm 0.2 \text{ mm s}^{-1}$. It is this eastward canyon transport that supplies fluid for the diapycnal upwelling.

c. Mixing rates and flow in an abyssal canyon

A fundamental feature of the abyssal Brazil Basin is the system of crests and canyons associated with the FZs of the MAR. Many canyons run zonally for hundreds of kilometers, and each canyon is bounded to the north and south by crests extending 500 to 1000 m above the canyon floors. The meridional wavelength of the canyon–crest system is roughly 30–50 km, and because of this the flow in these FZs was difficult to resolve in the inverse model calculations. Instead, each canyon is better modeled locally so that the special geometry of the system can be considered.

Consider the integral equations for advection of potential temperature and mass in a density layer bounded latitudinally by canyon walls. If the density layer is bounded by a density surface that intersects the canyon bottom to the east, then the control-volume budgets for heat and mass are

$$-\iint dy dz \bar{u} \bar{\Theta} + \iint dx dy \bar{w}_* \bar{\Theta} = -\iint dx dy F_\theta, \quad (14)$$

$$-\iint dy dz \bar{u} + \iint dx dy \bar{w}_* = 0. \quad (15)$$

Here, the $dydz$ integrals are evaluated at the western edge of the control volume, and the $dx dy$ integrals are taken along a surface of constant density. We can algebraically solve expressions (14) and (15) for an along-canyon flow rate \bar{u} if we express the cross-canyon integrals in simplified forms. We take $\iint dy dz \bar{u} = \bar{u} A_{(yz)}$ and $\iint dy dz \bar{u} \bar{\Theta} = \bar{u} \bar{\Theta}_{(yz)} A_{(yz)}$, where $A_{(yz)}$ is the area of the cross-canyon section and $\bar{\Theta}_{(yz)}$ is the cross-section weighted average of potential temperature. We may also treat the bounding isopycnal as a surface of nearly constant temperature $\bar{\Theta}_{(xy)}$ of area $A_{(xy)}$. This allows us to express the flow rate as

$$\bar{u} \cong \frac{A_{(xy)} \langle \Gamma \bar{\epsilon} N^{-2} \bar{\Theta}_z \rangle}{A_{(yz)} (\bar{\Theta}_{(xy)} - \bar{\Theta}_{(yz)})}, \quad (16)$$

where the thermal flux has been expressed as $F_\theta = -\Gamma \bar{\epsilon} N^{-2} (\partial \bar{\Theta} / \partial z)$.

This expression was evaluated using data from the section of HRP profiles shown in [Fig. 12](#) for the density layer with $\gamma_n > 28.20$. The diffusivities along the $\gamma_n = 28.20$ isopycnal were estimated as the ensemble average $k_\rho = \langle \Gamma \bar{\epsilon} (h = h_\sigma) N^{-2} \rangle$, across the canyon width, down the length of the canyon. Error analyses for the k_ρ estimates were done using Monte Carlo methods incorporating an uncertainty of ± 100 m in the bottom depth, along with the statistical uncertainty in $\bar{\epsilon}(h_{ab})$. Heat fluxes across the $\gamma_n = 28.20$ surface are roughly $-1 \times 10^{-6} \text{ m}^\circ\text{C s}^{-1}$, with the largest values at the eastern end. While the easternmost edge of the $\gamma_n = 28.20$ surface experiences the largest mixing rates, the stratification there was very weak ($N^2 = 6 \times 10^{-8} \text{ s}^{-2}$), keeping the buoyancy flux in this area comparable to fluxes occurring where mixing rates are weaker. These mixing rates are used in (16) and yield an up-canyon flow rate of $\bar{u} = (3.5 \pm 1) \text{ mm s}^{-1}$ at the western edge of the control volume. This result can be compared with the inverse estimates of $(0.4 \pm 0.2) \text{ mm s}^{-1}$ up-canyon flow. The apparent discrepancy is resolved if volume transports are compared rather than flow rates. The inverse model estimate utilized a subsampled bathymetric grid, such that the dimensions of canyons are only coarsely resolved. The canyon width was 55 km over the entire canyon's depth, giving $3 \times 10^7 \text{ m}^2$ as a typical cross section. The estimate from (16) of canyon flow relied on more careful estimates of roughly $5.5 \times 10^6 \text{ m}^2$ for canyon cross section. Therefore, the inverse estimates of volume transport are $(0.012 \pm 0.006) \times 10^6 \text{ m}^3 \text{ s}^{-1}$, while the section-derived estimate is $(0.019 \pm 0.005) \times 10^6 \text{ m}^3 \text{ s}^{-1}$. The two estimates are indistinguishable at the significance level of one standard error.

Net diapycnal upwelling is required across the $\gamma_n = 28.20$ surface between 18° and 16.5°W . From mass conservation

(15), the average diapycnal advection across $\gamma_n = 28.20$ in the canyon is $\bar{w}_* = (A_{(yz)}/A_{(xy)})\bar{u} = (230 \pm 70) \text{ m yr}^{-1}$.

d. Deep upwelling and mixing efficiency

As presented above, strong diapycnal upwelling is required to close the heat and mass budgets in the canyons. [Figure 13](#) presents a comparison of the a priori estimates of w_* to the inverse solutions for w_* on the $\gamma_n = 28.20$ neutral surface. Inverse estimates are generally consistent with the a priori estimates of w_* at sites where the $\gamma_n = 28.20$ surface is more than 300 m above the bottom. However, the inverse estimates suggest diapycnal upwelling is favored at sites where the $\gamma_n = 28.20$ surface is within 300 m of the bottom.

Diapycnal upwelling must be occurring in regions where turbulence supports a convergent buoyancy flux: $w_* N^2 \cong -\partial J_b / \partial z > 0$. This condition is satisfied by turbulence occurring close to the bottom since the buoyancy flux must decrease with depth to meet a no-flux condition at the seafloor. Within the context of (3), the buoyancy flux is related to the dissipation rate by a mixing efficiency parameter, $J_b = -\Gamma \epsilon$. We believe that a reduction in mixing efficiency near the bottom allows the no-flux condition to be met at the seafloor. This reduction may occur in a 1 to 10 m thick boundary layer (i.e., the “log layer”), which was unresolved by our measurements. However, variations in mixing efficiency may extend to greater heights in the canyons. The physical mechanisms controlling the efficiency of mixing near topography are not well understood, but turbulent mixing in regions enclosed by topography may favor mixing with reduced efficiency. [Stigebrandt and Aure \(1989\)](#) found that mixing in fjords occurred at 0.05 efficiency. Given our observations of dissipation and stratification along canyon slopes, a decrease in mixing efficiency from 0.2 to 0.05 in the bottom-most 100 m above FZ slopes would account for diapycnal upwelling as large as $w_* \cong +300 \text{ m yr}^{-1}$.

5. Discussion

This work has examined the buoyancy forcing and circulation occurring in a region of the abyssal ocean. Turbulent mixing is enhanced over the rough bathymetry near the MAR and its associated FZs, and this leads to enhanced diapycnal advection in these regions. Furthermore, the vortex stretching achieved by this diapycnal advection serves a significant role in the local balance of potential vorticity.

The signal of abyssal dissipation was found to have both spatial and temporal content. The spatial distribution of dissipation along an isopycnal is clearly related to bottom proximity. In the context of the complex bottom topography associated with FZs, dissipation profiles were found to have differing character for three classes of bathymetry. While dissipation generally increases toward the bottom, levels occurring over the flanks of sloping bathymetry exceed levels occurring on FZ crests and the floors of canyons. These spatial trends accompany a temporal modulation of dissipation, correlated with the spring–neap tidal cycle. An attempt was made to model these spatial and temporal trends, and the resulting model features a dependence with h_{ab} specific to the bathymetric classes of crests, canyons, and slopes. The temporal variability of dissipation was modeled according to a u^2 energy flux scaling of linear internal waves.

The modeled dissipation profiles were employed in an inverse model that combines their thermodynamic information with the dynamic constraints implied by the beta spiral and hydrographic budgets. Specifically, the dissipation rate model was used to provide both a measure of the diapycnal diffusivity k_ρ and an a priori estimate of the diapycnal advection w_* . This approach proved highly effective in resolving both the isopycnal and diapycnal components of flow.

a. Local consequences of buoyancy forcing

The results of the inverse calculation suggest that, while diabatic flow is weak in much of the interior, stronger levels of turbulence above rough bathymetry lead to enhanced levels of diabatic flow. Divergence of the diabatic flow acts as a mechanism of buoyancy forcing for the lateral circulation though the vortex stretching term $(f/h)(w_*(z_u) - w_*(z_l))$ in the vorticity budget. The significance of diabatic vortex stretching as a forcing mechanism must be assessed relative to other forcing agents for the flow. From the inverse estimates, we may compare the strength of buoyancy forcing to the adiabatic mechanism of vortex stretching, represented by $(f/h)\mathbf{u} \cdot \nabla \mathbf{h}$ in the vorticity budget.

In the deep density layers, adiabatic vortex stretching is cyclonic, while diabatic vortex stretching is anticyclonic. In the region where mixing rates are largest, these two mechanisms are comparable in magnitude, and the vortex stretching terms in (2) nearly cancel. Since $\beta \mathbf{v} \cong 0$, there is little meridional flow just above the level of FZ crests ([Figs. 6 and 7](#)). In addition to the stretching mechanisms, friction imposed by topography may also be a significant forcing mechanism near the bottom, though we have not attempted to assess this contribution. Farther west of the Mid-Atlantic Ridge where mixing rates are weaker, the adiabatic stretching exceeds the diabatic stretching, resulting in the southward flow where the largest

lateral velocities occur.

[Spall \(2001\)](#) has examined the planetary geostrophic dynamics for a circulation driven by buoyancy forcing over sloping topography. In his model, Spall represents only the large-scale zonal slope of FZ topography, with diapycnal upwelling from FZ canyons represented as flow out of the sloping bottom. Spall finds that bottom pressure torque tends to balance the diabatic vortex stretching in the deepest density layer, keeping the flow along the bottom weak even when the buoyancy forcing is strong.

To produce a clearer summary of the deep circulation near canyons, a zonal streamfunction (ψ) was defined by latitudinally integrating the velocity so that $\bar{u}\delta_y = -\psi_z$ and $\bar{w}_*\delta_y = \psi_x$, where the latitudinal limits of integration were taken over the inverse domain (19°–25°S),

$$\bar{u}(x, z) = \frac{1}{\int dy} \int dy u(x, y, z),$$

$$\bar{w}_*(x, z) = \frac{1}{\int dy} \int dy w_*(x, y, z).$$

The inverse model grid is coarsely spaced in depth, so an objective analysis technique ([Bretherton et al. 1976](#)) was used to interpolate the inverse solution and compute the streamfunction. Prior to the objective analysis, the grid coordinates were nondimensionalized by the assumed correlation scales. For the vertical dimension, the advective–diffusive scale $\hat{z} = k/w_* \cong 300$ m was used, while twice the baroclinic deformation radius was used for a lateral scale, $\hat{x} = 2Rd \cong 30$ km. The autocorrelation of the streamfunction was specified to e fold over three nondimensional correlation radii, $\hat{r}^2 = (z/\hat{z})^2 + (x/\hat{x})^2$. The resulting smoothed streamfunction is shown in [Fig. 14](#) relative to representative bathymetry and the density field. The circulation shallower than 3500 m is characterized by westward flow and diapycnal flow that is downward, while deeper flow is characterized by diapycnal upwelling at the eastern ends of canyons feeding westward flow at the level of the FZ crests. The streamfunction estimates were not extended deeper than 5000 m, as the objective mapping loses skill near the canyon floors. However, the diapycnal upwelling east of 18°W indicated by ψ at 5000 m is consistent with the eastward canyon flow resolved coarsely in the inverse model solution.

The net transport through a density surface (T_σ) can be expressed in terms of the streamfunction as $T_\sigma = \psi(x_w) - \psi(x_e)$, where (x_e, x_w) are the eastern and western limits of the surface area integral. The transport calculation is simplified if the eastern limit is taken to be the longitude where the surface incrops along the bottom, so that $\psi(x_e) = 0$. For the $\gamma_n = 28.20$ ($\sigma_4 = 45.98$ and $\theta \cong 0.8^\circ\text{C}$) surface, the net diapycnal transport between 19° and 25°S is $(0.34 \pm 0.14) \times 10^6 \text{ m}^3 \text{ s}^{-1}$. This is the integrated upwelling over 6° of latitude; the actual upwelling occurs in the canyons. Assuming that an up-canyon flow of 3.5 mm s^{-1} is typical of canyons that are 500 m deep and 30 km wide, then six or seven canyons would carry the required mass for upwelling. This is consistent with the number of canyons in the region.

b. Consequences for the basin-scale mass budget

Maps of seafloor bathymetry show a network of 20–30 FZs occupying the entire meridional extent of the Brazil Basin. Additionally, the character of barotropic tidal energy does not vary significantly along the axis of the MAR. Treating these as proxies for turbulent dissipation, the spatial distribution of mixing depicted in [Fig. 2](#) may be characteristic of the FZs throughout the greater basin. This would imply that buoyancy forcing plays an important role in driving the abyssal circulation. Indeed, [O'Dwyer and Williams \(1997\)](#) have produced basin-scale maps of $q = f/h$ that show that the streamfunction for adiabatic flow in the Brazil Basin is blocked by boundaries at depths greater than 3500 m. Flow in regions of blocked q contours occurs only under the action of buoyancy forcing and friction.

Some basin-scale consequences of abyssal buoyancy forcing are examined by considering the mass budget for water of temperature class $\theta < 0.8^\circ\text{C}$ in the Brazil Basin. This budget was considered by [Hogg et al. \(1982\)](#) and [Morris et al. \(2001\)](#). [Morris et al. \(2001\)](#) find that $(3.7 \pm 1.7) \times 10^6 \text{ m}^3 \text{ s}^{-1}$ of net upwelling occurs across the $\theta = 0.8^\circ\text{C}$ isotherm surface in the latitude range between 30°S and the equator. If the circulation shown in [Fig. 14](#) is characteristic of other FZ regions, a simple scaling of our localized estimate (6° of latitude) for net upwelling to the basin scale (30° of latitude) suggests an

upwelling across $\theta = 0.8^\circ\text{C}$ isotherm of $(1.7 \pm 0.7) \times 10^6 \text{ m}^3 \text{ s}^{-1}$. This number is in the general range needed to close the basin-scale mass budget.

The various regions of bottom water circulation in the Brazil Basin are shown in [Fig. 15](#). Bottom water enters the basin through the Vema Channel, and a boundary current carries this deep water northward along the western portion of the basin ([Reid 1989](#); [Speer and Zenk 1993](#); [Durrieu De Madron and Weatherly 1994](#)). However, over much of the zonal band between 35° and 25°W , FZs are absent and mixing levels and isopycnal slopes are likely to be small, so the mean flow should satisfy $\beta\mathbf{v} \cong 0$. Indeed, float observations in this region suggest that the flow is dominantly zonal ([Hogg and Owens 1999](#)). Farther to the east, mixing levels and isopycnal slopes increase above FZ topography. In this region, our inverse results serve as an example, and diapycnal advection will influence the lateral flow through the vorticity relation $\beta\mathbf{v} = (f/h)\mathbf{u} \cdot \nabla h + f(\partial w^*/\partial z)$. Net diapycnal upwelling of water masses colder than $\theta \cong 0.8^\circ\text{C}$ likely occurs in FZ canyons. Inversion of observations from January 1996 to April 1997 indicate a net southward transport of $-(0.34 \pm 0.05) \times 10^6 \text{ m}^3 \text{ s}^{-1}$ for the water class denser than $\gamma_n > 28.08$ in the boxed region ([Fig. 15](#)), though recent float observations suggest that meridional flows in this region are time varying (N. Hogg 2001, personal communication).

The work described here demonstrates that direct measures of mixing can be combined with hydrographic observations to give an estimate for circulation that is consistent with other large-scale budgets. This is in contrast to many earlier attempts to reconcile local dissipation estimates with mixing rates inferred from advective–diffusive budgets. A notable difference between the current approach and early treatments of dissipation data rests with the application of an inverse technique with both microstructure and conventional hydrographic data. While direct observations of mixing tend to give detailed information on local diapycnal exchange processes, hydrographic budgets predict only the mean of diabatic forcing over large scales. Neither approach alone would give a meaningful measure of the full three-dimensional circulation.

Buoyancy forcing provided by turbulent mixing likely provides the dominant forcing for the abyssal circulation, and the highly localized observations described here constitute the only available observations of deep dissipation. The localized measurements presented here suggest that the spatial structure of abyssal buoyancy forcing is far richer than Stommel and Aron's example of uniform upwelling.

Acknowledgments

We thank Kurt Polzin and Jim Ledwell for helpful discussions during the preparation of this manuscript. The authors also thank Ellyn Montgomery, Dave Wellwood, and Tom Bolmer, and the officers and crew of the R/V *Seward Johnson* for support of our field program. Comments from Chris Garrett, Nelson Hogg, Trevor McDougall, Mike Spall, and two anonymous reviewers improved this presentation. This work was supported by Grant OCE94-15589 of the National Science Foundation. The support of the Office of Naval Research is also acknowledged.

REFERENCES

- Baines P. G., 1982: On internal tide generation models. *Deep-Sea Res.*, **29**, 307–338. [Find this article online](#)
- Barton E. D., and A. E. Hill, 1989: Abyssal flow through the Amirante Trench (Western Indian Ocean). *Deep-Sea Res.*, **36**, 1121–1126. [Find this article online](#)
- Bell T. H., 1975: Lee waves in stratified flows with simple harmonic time dependence. *J. Fluid Mech.*, **67**, 705–722. [Find this article online](#)
- Bevington P. R., and D. K. Robinson, 1992: *Data Reduction and Error Analysis for the Physical Sciences*. McGraw-Hill, 328 pp.
- Bretherton F. P., R. E. Davis, and C. B. Fandry, 1976: A technique for objective analysis and design of oceanographic experiments applied to MODE-73. *Deep-Sea Res.*, **23**, 559–582. [Find this article online](#)
- Durrieu De Madron X., and G. Weatherly, 1994: Circulation, transport and bottom boundary layers of the deep currents in the Brazil Basin. *J. Mar. Res.*, **52**, 583–638. [Find this article online](#)
- Efron B., and G. Gong, 1983: A leisurely look at the bootstrap, the jackknife, and cross-validation. *Amer. Stat.*, **37**, 36–48. [Find this article online](#)
- Egbert G. D., A. F. Bennett, and M. G. G. Foreman, 1994: TOPEX/POSEIDON tides estimated using a global inverse model. *J. Geophys. Res.*, **99**, 24821–24852. [Find this article online](#)
- Fukumori I., 1991: Circulation about the Mediterranean Tongue: An analysis of an EOF-based model ocean. *Progress in Oceanography*, Vol. 27, Pergamon, 197–224.

- Garrett C., 2001: An isopycnal view of near-boundary mixing and associated flows. *J. Phys. Oceanogr*, **31**, 138–142. [Find this article online](#)
- Gill A. E., 1982: *Atmosphere–Ocean Dynamics*. Academic Press, 662 pp.
- Hautala S. L., and S. C. Riser, 1993: A nonconservative β -spiral determination of the deep circulation in the Eastern South Pacific. *J. Phys. Oceanogr*, **23**, 1975–2000. [Find this article online](#)
- Hogg N. G., and W. B. Owens, 1999: Direct measurements of the deep circulation within the Brazil Basin. *Deep-Sea Res. II*, **46**, 335–353. [Find this article online](#)
- Hogg N. G., P. Biscaye, E. Gardner, and W. J. Schmitz, 1982: On the transport of Antarctic Bottom Water in the Verma Channel. *J. Mar. Res.*, **40**, 231–263, (Suppl). [Find this article online](#)
- Huq P., and R. E. Britter, 1995: Turbulence evolution and mixing in a two layer stably stratified fluid. *J. Fluid Mech*, **285**, 41–67. [Find this article online](#)
- Ivey G. N., and J. Imberger, 1991: On the nature of turbulence in a stratified fluid. Part I: The energetics of mixing. *J. Phys. Oceanogr*, **21**, 650–658. [Find this article online](#)
- Jackett D. R., and T. J. McDougall, 1997: A neutral density variable for the world's oceans. *J. Phys. Oceanogr*, **27**, 237–263. [Find this article online](#)
- Kunze E., and T. B. Sanford, 1996: Abyssal mixing: Where it is not. *J. Phys. Oceanogr*, **26**, 2286–2296. [Find this article online](#)
- Ledwell J. R., E. T. Montgomery, K. L. Polzin, L. C. St. Laurent, R. W. Schmitt, and J. M. Toole, 2000: Mixing over rough topography in the Brazil Basin. *Nature*, **403**, 179–182. [Find this article online](#)
- Menke W., 1989: *Geophysical Data Analysis: Discrete Inverse Theory*. Academic Press, 285 pp.
- McDougall T. J., 1987: Thermobaricity, cabbeling, and water-mass conversion. *J. Geophys. Res.*, **92**, 5448–5464. [Find this article online](#)
- McDougall T. J., 1988: Neutral-surface potential vorticity. *Progress in Oceanography*, Vol. 20, Pergamon, 185–221.
- McDougall T. J., 1995: The influence of ocean mixing on the absolute velocity vector. *J. Phys. Oceanogr*, **25**, 705–725. [Find this article online](#)
- Morris M., M. M. Hall, L. C. St. Laurent, and N. Hogg, 2001: Abyssal mixing in the Brazil Basin. *J. Phys. Oceanogr*, **31**, 3331–3348.
- Moum J. N., 1996: Efficiency of mixing in the main thermocline. *J. Geophys. Res.*, **101**, 12057–12069. [Find this article online](#)
- O'Dwyer J., and R. G. Williams, 1997: The climatological distribution of potential vorticity over the abyssal ocean. *J. Phys. Oceanogr*, **27**, 2488–2506. [Find this article online](#)
- Osborn T. R., 1980: Estimates of the local rate of vertical diffusion from dissipation measurements. *J. Phys. Oceanogr*, **10**, 83–89. [Find this article online](#)
- Pedlosky J., 1996: *Ocean Circulation Theory*. Springer-Verlag, 453 pp.
- Polzin K. L., and E. T. Montgomery, 1996: Microstructure profiling with the high resolution profiler. *Proc. ONR Workshop on Microstructure Sensors*, Mt. Hood, OR, Office of Naval Research, 109–115.
- Polzin K. L., J. M. Toole, J. R. Ledwell, and R. W. Schmitt, 1997: Spatial variability of turbulent mixing in the abyssal ocean. *Science*, **276**, 93–96. [Find this article online](#)
- Reid J. L., 1989: On the total geostrophic circulation of the South Atlantic Ocean: Flow patterns, tracers, and transports. *Progress in Oceanography*, Vol. 23, Pergamon, 149–244.
- Roemmich D., S. Hautala, and D. Rudnick, 1996: Northward abyssal transport through the Samoan Passage and adjacent regions. *J. Geophys Res.*, **101**, 14039–14055. [Find this article online](#)
- Saunders P. M., 1987: Flow though Discovery Gap. *J. Phys. Oceanogr*, **17**, 631–643. [Find this article online](#)
- Schmitt R. W., J. M. Toole, R. L. Koehler, E. C. Mellinger, and K. W. Doherty, 1988: The development of a fine- and microstructure profiler. *J. Atmos. Oceanic Technol*, **5**, 484–500. [Find this article online](#)
- Smith W. H. F., and D. T. Sandwell, 1997: Global sea floor topography from satellite altimetry and ship depth soundings. *Science*, **277**,

1956–1962. [Find this article online](#)

Spall M. A., 2001: Large-scale circulations forced by localized mixing over a sloping bottom. *J. Phys. Oceanogr.* **31**, 2369–2384.

Speer K. G., and W. Zenk, 1993: The flow of Antarctic Bottom Water into the Brazil Basin. *J. Phys. Oceanogr.* **23**, 2667–2682. [Find this article online](#)

Speer K. G., G. Siedler, and L. Talley, 1995: The Namib Col Current. *Deep-Sea Res.* **42**, 1933–1950. [Find this article online](#)

Stigebrandt A., and J. Aure, 1989: Vertical mixing in basin waters of fjords. *J. Phys. Oceanogr.* **19**, 917–926. [Find this article online](#)

St. Laurent L., 1999: Diapycnal advection by double diffusion and turbulence in the ocean. Ph. D. dissertation, MIT–WHOI Joint Program in Oceanography, 139 pp.

St. Laurent L., and R. W. Schmitt, 1999: The contribution of salt fingers to vertical mixing in the North Atlantic Tracer Release Experiment. *J. Phys. Oceanogr.* **29**, 1404–1424. [Find this article online](#)

Stommel H., 1957: The abyssal circulation of the ocean. *Nature*, **180**, 733–734. [Find this article online](#)

Stommel H., and A. B. Arons, 1960: On the abyssal circulation of the World Ocean—I: Stationary planetary flow patterns on a sphere. *Deep-Sea Res.* **6**, 140–154. [Find this article online](#)

Stommel H., and F. Schott, 1977: The beta spiral and the determination of the absolute velocity field from hydrographic station data. *Deep-Sea Res.* **24**, 325–329. [Find this article online](#)

Stommel H., A. B. Arons, and A. J. Faller, 1958: Some examples of stationary planetary flow patterns in bounded basins. *Tellus*, **10**, 1–11. [Find this article online](#)

Toole J. M., K. L. Polzin, and R. W. Schmitt, 1994: Estimates of diapycnal mixing in the abyssal ocean. *Science*, **264**, 1120–1123. [Find this article online](#)

Toole J. M., R. W. Schmitt, K. L. Polzin, and E. Kunze, 1997a: Near-boundary mixing above the flanks of a midlatitude seamount. *J. Geophys. Res.* **102**, 947–959. [Find this article online](#)

Toole J. M., J. R. Ledwell, K. L. Polzin, R. W. Schmitt, E. T. Montgomery, L. St. Laurent, and W. B. Owens, 1997b: The Brazil basin Tracer Release Experiment. *Int. WOCE Newslett.* **28**, 25–28. [Find this article online](#)

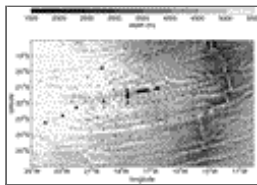
Whitehead J. A., and L. V. Worthington, 1982: The flux and mixing rates of Antarctic Bottom Water within the North Atlantic. *J. Geophys. Res.* **87**, 7903–7924. [Find this article online](#)

Wunsch C., 1996: *The Ocean Circulation Inverse Problem*. Cambridge University Press, 442 pp.

Yamazaki H., and T. R. Osborn, 1990: Dissipation estimates for stratified turbulence. *J. Geophys. Res.* **95**, 9739–9744. [Find this article online](#)

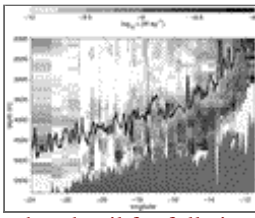
Zhang H.-M., and N. G. Hogg, 1992: Circulation and water mass balance in the Brazil Basin. *J. Mar. Res.* **50**, 385–420. [Find this article online](#)

Figures



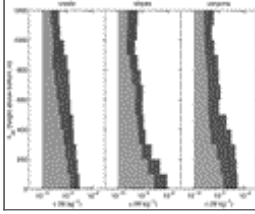
[Click on thumbnail for full-sized image.](#)

FIG. 1. Map of the BBTRE site with the 2 arc-minute resolution bathymetric estimates of [Smith and Sandwell \(1997\)](#). A total of 129 profiles of dissipation rate data were used from HRP observations made during 1996 (triangles) and 1997 (crosses)



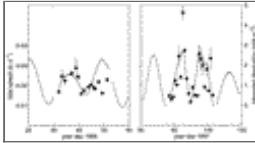
[Click on thumbnail for full-sized image.](#)

FIG. 2. A zonal section of TKE dissipation rate ϵ . The individual profiles are shown as columns, and dissipation rate observations were vertically averaged into 100-m bins. The shaded bathymetry is representative of canyon floors, while the shallower trace represents the level of FZ crests. Hatch marks indicate regions with no data



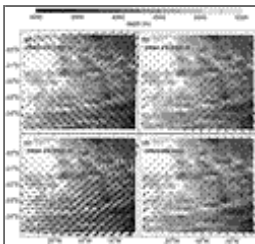
[Click on thumbnail for full-sized image.](#)

FIG. 3. Dissipation profiles averaged according to the local bathymetry classification. Bathymetric classes were assigned as crests, canyons, or slopes. All profiles are shown relative to a reference dissipation of $\epsilon = 1 \times 10^{-10} \text{ W kg}^{-1}$. The 95% confidence interval is shown for each 100-m average



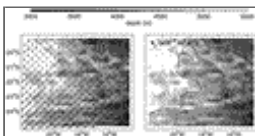
[Click on thumbnail for full-sized image.](#)

FIG. 4. Comparison of column-integrated dissipation with the local daily averaged tidal speed. The tidal velocity record was produced by the TPXO model of [Egbert et al. \(1994\)](#), and estimates were made along the survey tracks. Tidal estimates at a central location (21°S , 18.5°W) were used for time intervals preceding and following survey periods. The dissipation estimates $\rho\epsilon$ were integrated to $h_{\text{ab}} = 2000 \text{ m}$, and daily averages with standard errors are shown



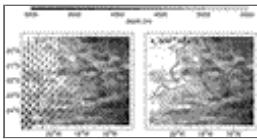
[Click on thumbnail for full-sized image.](#)

FIG. 5. Layer-averaged geostrophic flow for the density layers $27.60 < \gamma_n < 27.97$ (a), $27.97 < \gamma_n < 28.04$ (b), $28.04 < \gamma_n < 28.08$ (c), and the reference level (d). The largest vectors correspond to speeds of 2 mm s^{-1} . At each estimation point 10 alternate estimates are shown from the Monte Carlo set of 50-m perturbations to the isopycnal-height field. The mean layer depth is reported in the corner of each panel



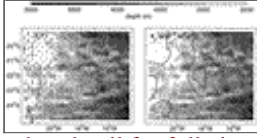
[Click on thumbnail for full-sized image.](#)

FIG. 6. Layer-averaged flow (left) and diapycnal diffusivities (right) for the density layer $28.08 < \gamma_n < 28.16$ ($45.83 < \sigma_4 < 45.94$). The average flow speed is 3 mm s^{-1} . Turbulent diffusivities are shown for the central surface $\gamma_n = 28.12$, and contour values reflect $1^\circ \times 1^\circ$ averaging. Regions where flow is blocked by topography are included in the averaging



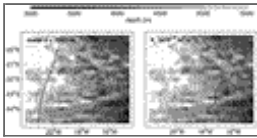
[Click on thumbnail for full-sized image.](#)

FIG. 7. Layer-averaged flow and diapycnal diffusivities for the density layer $28.16 < \gamma_n < 28.20$ ($45.94 < \sigma_4 < 45.99$). Southward and westward flow characterizes the western half of the region with speeds 4 to 6 mm s^{-1} . Turbulent diffusivities are shown for the central surface $\gamma_n = 28.18$



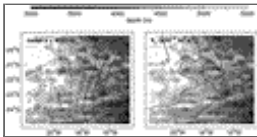
[Click on thumbnail for full-sized image.](#)

FIG. 8. Layer-averaged flow and diapycnal diffusivities for the density class $\gamma_n > 28.20$ ($\sigma_4 > 45.99$). The scale of the vectors is enhanced relative to [Figs. 6 and 7](#), and the magnitude of the southward flow on the western edge of the region is 2 to 4 mm s^{-1} . Estimates of flow in FZ canyons are eastward with magnitude 0.2 to 0.5 mm s^{-1} . Turbulent diffusivities are shown for the surface $\gamma_n = 28.22$



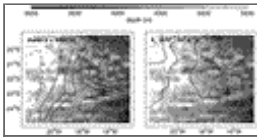
[Click on thumbnail for full-sized image.](#)

FIG. 9. Diapycnal advection (left panel) and diapycnal diffusivities (right panel) on the $\gamma_n = 28.08$ surface ($\sigma_4 = 45.83$). Contoured values for both quantities reflect $1^\circ \times 1^\circ$ averaging in cells that include regions blocked by topography



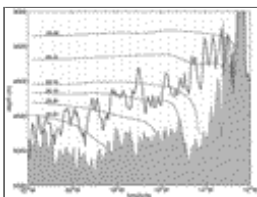
[Click on thumbnail for full-sized image.](#)

FIG. 10. Diapycnal advection and diffusivities on the $\gamma_n = 28.16$ surface ($\sigma_4 = 45.94$). Downward advection dominates the portion of the region west of 18° , while upwelling is estimated in the eastern region where FZ crests are abundant. Uncertainties of the w_* estimates on this surface are roughly $\pm 20\%$ of the contoured values



[Click on thumbnail for full-sized image.](#)

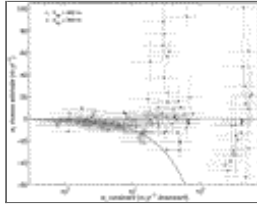
FIG. 11. Diapycnal advection and diffusivities on the $\gamma_n = 28.20$ surface ($\sigma_4 = 45.98$). Upward advection dominates the surface, and uncertainties of these w_* estimates are roughly $\pm 40\%$ of the contoured values



[Click on thumbnail for full-sized image.](#)

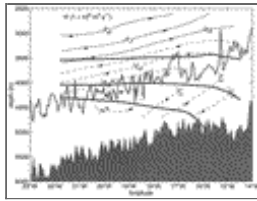
FIG. 12. Density section in the unnamed canyon near 22°S . Contours of neutral density γ_n are shown, but equivalent values of σ_4 can be found in the text. The observed data were averaged vertically and horizontally to produce the field shown. Shaded

bathymetry is the canyon floor, while the bathymetric trace (gray line) shows the average depth of the canyon walls. Isopycnals denser than $\gamma_n > 28.12$ intersect to floor of the canyon. Dotted vertical lines denote station profiles



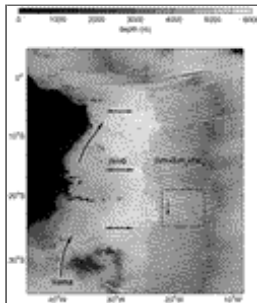
[Click on thumbnail for full-sized image.](#)

FIG. 13. Comparison of the a priori estimates of w^* with the inverse estimates for the $\gamma_n = 28.20$ ($\sigma_4 = 45.99$) neutral density surface. Estimates at sites where the $\gamma_n = 28.20$ surface is more than 300 m above the bottom are plotted using triangles, and estimates from sites where $\gamma_n = 28.20$ is less than 300 m above the bottom are plotted as points. The curve along which the inverse and a priori estimates are equal is shown. Standard errors are shown for all estimates



[Click on thumbnail for full-sized image.](#)

FIG. 14. The meridionally integrated streamfunction as estimated through objective analysis of the inverse model solution. Dimensional values of the streamfunction are contoured, and uncertainties are roughly $\pm 40\%$. Representative bathymetry of the canyon floors (shaded) and crests (gray line) is shown, as are the $\gamma_n = 28.10$, 28.16, and 28.20 isopycnals



[Click on thumbnail for full-sized image.](#)

FIG. 15. Schematic of hypothetical circulation of AABW with temperature class $\Theta < 0.8^\circ\text{C}$. Deep waters enter the through the Vema passage at the southwest corner of the basin, but do not leave the basin adiabatically. A western boundary current transports deep water northward. East of the boundary current, but west of FZs, flow is predominantly zonal and satisfies the vorticity equation $\beta\mathbf{U} \cong 0$. Above FZs (hatched region east of 25°W), mixing levels and isopycnal slopes increase and the advection of potential vorticity is balanced by both adiabatic and diabatic vortex stretching. A box is drawn around the region examined by inverse methods in this study. Net southward transport of AABW was found in this region during the 1996–97 observation period

* Woods Hole Oceanographic Institution Contribution Number 10478.

Corresponding author address: Louis C. St. Laurent, School of Earth and Ocean Sciences, University of Victoria, Victoria, BC V8W 3P6, Canada.
E-mail: lous@uvic.ca



© 2008 American Meteorological Society [Privacy Policy and Disclaimer](#)

Headquarters: 45 Beacon Street Boston, MA 02108-3693

DC Office: 1120 G Street, NW, Suite 800 Washington DC, 20005-3826

amsinfo@ametsoc.org Phone: 617-227-2425 Fax: 617-742-8718

[Allen Press, Inc.](#) assists in the online publication of *AMS* journals.